IEEE Access
Multidisciplinary ⋮ Rapid Review ⋮ Open Access Journal

Received March 19, 2019, accepted April 4, 2019, date of publication April 11, 2019, date of current version April 24, 2019.

Digital Object Identifier 10.1109/ACCESS.2019.2910636

Synchronous Wireless Body Sensor Network Enabling Human Body Pose Estimation

DENNIS LAURIJSSEN[1,2,3], (Graduate Student Member, IEEE), WIM SAEYS[4], STEVEN TRUIJEN[2,4], WALTER DAEMS[1,2], (Senior Member, IEEE), AND JAN STECKEL[1,2,3]

[1]FTI CoSys Lab, University of Antwerp, 2020 Antwerp, Belgium
[2]Centre for Care Technology, University of Antwerp, 2610 Antwerp, Belgium
[3]Flanders Make Strategic Research Centre, 3920 Lommel, Belgium
[4]FMH REVAKI, University of Antwerp, 2610 Antwerp, Belgium

Corresponding author: Jan Steckel (jan.steckel@uantwerpen.be)

This work was supported in part by the Special Research Grant (BOF-STIMPRO) of the University of Antwerp.

ABSTRACT In this paper, a novel human body pose estimation system is introduced, which features a synchronous network of wirelessly connected sensor nodes, thus forming a wireless body sensor network (WBSN). This measurement architecture for establishing human body pose estimations works in combination with the HTC Vive base stations and a Wi-Fi router. The former emits infrared pulses and laser sweeps in the horizontal and vertical plane captured by the sensor nodes' photodiodes. The infrared data can be converted into an azimuth and elevation angle for each photodiode relative to the emitting HTC Vive device. To estimate the human body poses, the sensor data are fed into a probabilistic non-linear maximum likelihood estimator combined with a parametric human body model. Using a parametric human body model for estimating the poses proves to be more resilient to sensor noise compared to estimating the Six Degrees of Freedom (6DoF) of every sensor node individually. The solution space can be constrained to the parameters of the users body model that relates to *a priori* information on the subject. The combination of the proposed hardware sensor network, its synchronous sensor data, and processing algorithms yields a cost-efficient human body pose estimation system.

INDEX TERMS Body sensor networks, distributed embedded systems, motion capture, pose estimation, sensor arrays.

I. INTRODUCTION

The notion of Body Sensor Networks (BSN) might still seem like a futuristic science fiction concept, the reality however is that these types of devices are becoming more ubiquitous nowadays. Smartphones equipped with a wireless radio (e.g. Bluetooth) can easily connect to a great number of wireless or other so called ''smart'' peripherals. The medical sector is adopting this technology for closely and continuously monitoring some of the vital body functions in a less intrusive manner [1]–[3]. More commonly known examples of these BSNs have spurred a booming market of health, sports and fitness accessories e.g. wireless heart rate monitors, pedometers, stride length monitors, cadence meters, smart or sports watches that enable the user to monitor his/her physical health, sporting performance progression and sleeping patterns. Besides these devices, targeted at ambitious yet amateur athletes, the professional sporting sector has also taken its interest in this technology. The aforementioned devices all have their professional counterparts that feature either more accurate and precise measurements, have more features or both. Gathering correct information has become crucial for training efficiently. A factor that takes a great part in this is the athletes' form or technique [4]–[7]. In order to objectively quantify the relevant technical performance metrics, motion capture technology is being used to further refine this. Rehabilitation physicians and physiotherapists are currently also using motion capture technologies for full body pose estimation purposes [8]. By using full or partial body pose estimation to objectively quantify the gait of a rehabilitating patient, the rehabilitation process can be personalized and adjusted in a timely manner [9], [10]. This can significantly reduce the recovery time of the patient, hence shortening the time spent in a hospital or

The associate editor coordinating the review of this manuscript and approving it for publication was Pietro Savazzi.

rehabilitation center, and potentially reduce costs for all involved parties.

The best known method for establishing motion capture is vision based. Vision-based systems make use of specific passive or active markers that can be attached to the person or object combined with specialized cameras (e.g. ViCon or Qualisys) [11]–[13]. The downside is that the cost of these systems can range from €20.000 to €300.000. Markerless vision-based pose estimation systems using ''standard'' RGB cameras are also showing promising results when combined with machine-learning algorithms such as a Deep Neural Networks [14] or a Convolutional Neural Networks [15]. Another method for motion capture applications is a BSN of nodes that are equipped with Inertial Measurement Units (IMUs) [11], [16] and often a wireless radio. These nodes can be strapped to the various body parts or can be integrated into a specialized body suit (e.g. XSens) [17]–[21]. Since IMU devices inherently suffer from integration errors [22], [23], these type of sensors cannot be used to achieve high-accuracy and high-precision pose estimations without making certain assumption regarding human motion patterns that compensate for these errors. Therefore, using this setup in rehabilitation scenarios where normal gait patterns cannot be expected, is not feasible.

To overcome these issues, we propose a low-cost body sensor network which consists of wirelessly synchronized sensor nodes that are equipped with a variety of sensors based on our experience from previous work [24]–[27]. It constitutes an architecture that enables human body pose estimation. One of the sensor data sources of the WBSN nodes allows capturing infrared (IR) light pulses and sweeps emitted by HTC Vive base stations (also known as Lighthouses) that are installed in the environment. As shown in previous work [27], this technology allows us to achieve accuracies up to ±3 cm in position and ±6° in orientation estimates for single nodes while attaining sub-millimeter and sub-degree precision for the former and the latter. In our previous work we estimated the six Degrees-of-Freedom (6DoF) pose of the individual nodes, which consists of a 3D-position and 3D-orientation, and combined these poses to estimate a human body pose. In order to increase the accuracy, precision and robustness of the body pose estimations, we can model a human subject as a network of body parts, on which sensors nodes can be attached, interconnected by joints. The parameters of the model consist of the physical dimensions of these body parts, rotational ranges of the joints and placements of the sensors. By using this parametric human body model the solution space of the human body pose estimations can be reduced, which in turn should increase robustness, accuracy and precision of the proposed solution.

In section II, the hardware of the individual nodes will be presented, together with the sensor measurement and synchronization scheme. In section III the probabilistic approach for estimating the actual pose of the individual nodes will be discussed together with the human body model that combines the individual node estimates into a body pose estimation. This pose estimation technique is validated through simulation of which the results are shown in section IV. The results of the experiments that were performed with the combination of the aforementioned technology and techniques are presented in section V. In the final section we will discuss our conclusions for the proposed solution and future work. Additionally new functionalities that we want to explore in the future were also included.

II. SYSTEM TOPOLOGY

In order to achieve the proposed low-cost wireless body sensor network nodes, a hardware topology was defined that offers sufficient capabilities for ongoing and future research purposes. In the design, we took into account the deficiencies of earlier measurement hardware we developed.

A. HARDWARE ARCHITECTURE

The chosen hardware topology has to meet a number of prerequisites. In the first place, the overall system cost should remain low, i.e. approximately €1.000 for a WBSN that can provide full body pose estimates. Secondly, since the wireless sensor nodes need to be attached to various parts of a human body these devices need to be relatively small and light. Thirdly, every node needs to be able to function autonomously. In this case, this third prerequisite implies that the node should function as a stand-alone member of the wireless network as well as function without any (extra) cables for power or data transfers to ensure the test subject's normal movement ranges.

To support the autonomy of the WBSN nodes a trade-off has to be made in processing power and power consumption while maintaining a compact and viable solution. There is a great variety of micro-controllers and processors that are available nowadays ranging from tiny Integrated Circuits (ICs) that target ultra low-power applications to so called System-in-Package (SiP) ICs that basically embed an entire UNIX system. Somewhere in between these two extremes resides the ARM Cortex M4 series microcontrollers that incorporate numerous interfaces and hardware capabilities at a reasonable power consumption. Within the range of these M4-devices a great variety exists in features, clock speeds, pin-count, physical size and price. To check off all of the aforementioned prerequisites, an STM32F429 microcontroller from STMicroelectronics [28] was chosen as the core of the WBSN nodes. The main purposes for this microcontroller are sensor data acquisition, timekeeping and performing data transfers. Although the internal memory provides 128 kB of data storage, an extra external RAM IC of 8 MB was chosen. Using the on-board flexible memory controller, the external memory can be read or written just like the internal memory with only slightly slower transfer speeds. Given the size of this external memory, a large amount of data can be buffered in worst case scenarios were data transfers to other computers might not be feasible in real-time. Figure 1 illustrates how the various components of the hardware architecture are connected to each other. As one of the sensor

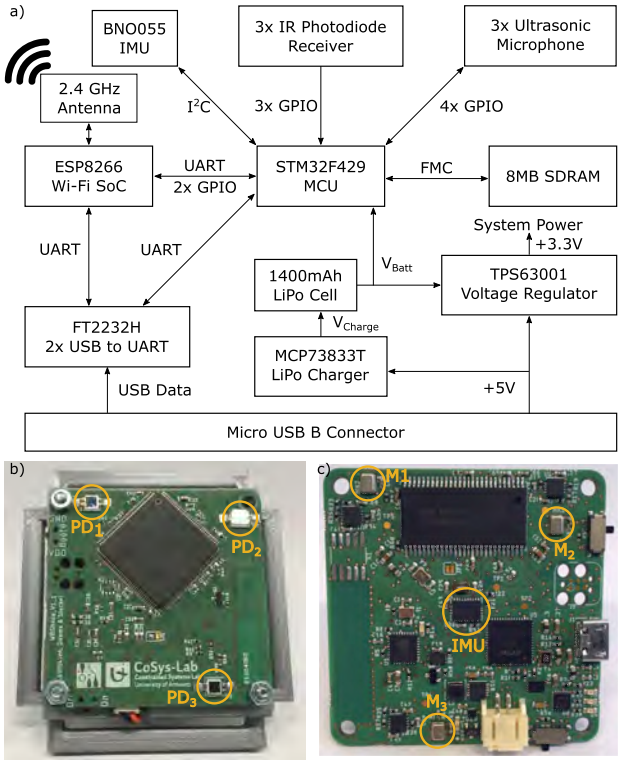

FIGURE 1. **Panel a) shows the schematic overview of the WBSN node that uses an STMicroelectronics STM32F4 microcontroller at its core. This ARM Cortex M4 microcontroller will perform the data acquisition of the HTC Vive base station infrared pulses and sweeps, of the Knowles ultrasound microphones and of the Bosch BNO055 Inertial IMU. The data can be stored in an external 8 MB RAM chip that serves as a data buffer before transferring the data to a central server through the Espressif ESP8266 Wi-Fi SoC or wired interface provided by the FTDI FT2232H IC. The latter converts a USB data connection to two UART interfaces that can be used for data transfers and reprogramming both microcontrollers. The USB connection also provides power to the system through the voltage regulator and the Microchip MCP73833T LiPo charge controller IC that in turn safely charges a connected single-cell LiPo battery. Panel b) shows the front side of the WBSN node on which the photodiode sensor elements are marked. The PCB is mounted on the 3D-printed enclosure that incorporates the 1400 mA h LiPo cell providing an autonomy of approximately 10 hours. The combination of the PCB and enclosure measures 6.8 by 7.2 by 1.85 cm and can be attached to objects or body parts. Panel c) shows the back side of the WBSN node where the digital microphones are marked together with the triaxial gyroscope, accelerometer and magnetometer IMU sensor which aligns to the center of the PCB.**

modalities of the WBSN nodes, a three-element infrared photodiode array was chosen in order to capture infrared pulses and sweeps emitted by two HTC Vive base stations. By accurately timing the rising and falling edges of these infrared emissions, the azimuth and elevation relative to the emitting base station can be calculated for every photodiode. This sensor modality was chosen because of the demonstrated efficacy for estimating 6DoF-poses of sensor nodes in our previous work [27], the low-cost of the receiver hardware and the off-the-shelve available HTC Vive base stations.

When working with spherical coordinates to represent a point in 3D-space, the HTC Vive system can provide the azimuth and elevation data whereas the distance can be estimated using the configuration of the photodiode array. Given our previous work [24]–[26], accurately measuring distance using ultrasound emissions is a feasible and low-cost solution. Therefore, a three-element digital microphone array [29] was fitted on the nodes. These Knowles SPH0641LU4H-1 [30] digital microphones incorporate an analog amplifier together with a 1-bit $\Sigma\Delta$ Analog-to-Digital Converter (ADC) in a single cost-efficient package. When introducing an ultrasound transmitter into the measurement environment at a known absolute location or relative position in regard to the HTC Vive base stations, the extra information can improve the pose estimates' robustness, accuracy and precision.

As a third sensor modality a Bosch BNO055 [31] IMU sensor was used in this hardware architecture. It can also be found in other rehabilitation and binaural hearing research [32]–[34]. This specific IMU integrates a triaxial gyroscope, accelerometer and magnetometer. It also features a small on-board microcontroller that can fuse this specific sensor data into absolute orientations (e.g. quaternions or Euler angles) using recursive Bayesian filtering techniques. Due to its ease of use, high-accuracy and data fusion capabilities this sensor can provide absolute orientation information of the sensor nodes at an increased data rate. Because of its intrinsic operation it can also alleviate Non-Line-Of-Sight (NLOS) situations of the optical and acoustic sensors that either yield no or inaccurate sensor data.

In order to wirelessly transfer the acquired sensor data to a central processing hub, the ubiquitous IEEE 802.11 wireless radio standard was chosen, commonly known as Wi-Fi. The one-to-many scalable network topology, high data throughput rate, possible internet access and off-the-shelve low-cost router hardware (if required) fits the envisioned system architecture. To create a Wi-Fi client out of a WBSN node, a low-cost and low-power Espressif ESP8266 [35] Wi-Fi System-on-Chip (SoC), which runs a full TCP/IP stack, was used together with an inverted-F PCB trace antenna tuned to 2.4 GHz. Since this SoC features a programmable microcontroller its operation can be tailored to cooperate with the STM32F4 in a joint state machine. Besides a wireless connection, a wired USB connection was also provided which serves multiple purposes. Firstly, the USB data is routed to an FTDI FT2232H IC which creates two Universal Asynchronous Receiver-Transmitter (UART) interfaces that connect to both the ESP8266 and the STM32F4 microcontrollers for either data transfers or reprogramming purposes. Secondly, the 5 V that is provided through the USB connection will provide power to the entire system and is used by the Microchip MCP73833T Lithium Polymer (LiPo) charge controller IC to safely charge single-cell LiPo batteries. The proposed system uses a 1400 mA h LiPo cell to provide power to the WBSN node for approximately 10 hours of continuous operation. This satisfies the autonomous measurement prerequisite or other use-cases where a USB connection is not available or feasible. In Figure 1 panel b) the actual assembled PCB is shown mounted on a 3D-printed enclosure that incorporates the LiPo battery. It can be strapped to an object or body part. The PCB fits all of the aforementioned ICs in a 5 by 5 cm rectangle. In combination with the

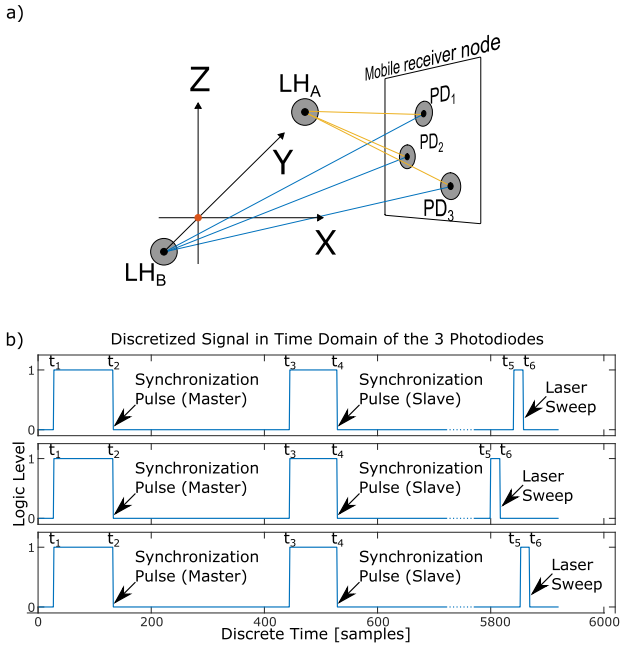

FIGURE 2. Panel a) illustrates two HTC Vive base stations (LH_A and LH_B placed in an environment together with a WSBN node that is equipped with three IR sensitive photodiodes that will receive the IR pulses emitted by LH_A and LH_B. b) shows three discretized photodiode receiver signals that exhibit two synchronization pulses, which are received at the same time, together with a narrow pulse that corresponds to the either the horizontal or vertical IR laser plane sweep that passes over the photodiode.

3D-printed enclosure a node measures 6.8 cm by 7.2 cm by 1.85 cm. When combining the price of the PCBs with the price of all components, the hardware cost of a single WBSN node amounts to approximately €65 (in a batch of 10 nodes). Fifteen of these sensors, adding up to ±€975, should suffice for estimating a full body pose. The €1000 price point is slightly exceeded when a Wi-Fi router and two HTC Vive base stations are added to the system cost. However, it is reasonable to assume that the sensor cost can be decreased significantly in a larger production quantity.

B. PROPOSED DATA ACQUISITION AND PROCESSING

As mentioned in the previous subsection, the WBSN nodes are equipped with three sensor modalities. Each sensor technology has its inherent advantages and disadvantages but can be combined to complement each other. However in this work, we will focus on a single sensor modality that will be used as the primordial source of data for establishing human body pose estimates. Other modalities will be added later in an iterative design process. Given the positive results of our previous work [27], the three-element photodiode array combined with two fixed HTC Vive base stations in a measurement environment were chosen to start from.

The three IR photodiodes are positioned on the WBSN PCB in an acute triangle configuration, as shown in Figure 1 panel b), and will receive the IR pulses and sweeps originating from the base stations, which is illustrated in Figure 2 panel a). To extract the azimuth and elevation information, also referred to as lighthouse data in this paper, the STM32F4 microcontroller registers the timing at which the rising and falling edges are detected. With two HTC Vive base stations the discretized photodiode receiver signal, shown in Figure 2 panel b), will exhibit a pulse train that features two sync pulses with varying pulse width and a narrow pulse that represents the passing of either the horizontal or vertical sweep. As will be detailed later, the delay between t_1 or t_3 and t_5 is affinely related to the azimuth and elevation angle under which the photodiode was swept by the laser plane. This delay differs for each photodiode due to their different positions on the PCB. The sequence of two synchronization pulses and a sweep occurs at a rate of 120 Hz. The duration of the synchronization pulse flashes encodes three information bits that indicate whether (a) the device will produce an IR laser sweep, whether (b) it will be the vertical or horizontal sweep and (c) an additional data bit. The latter can be used to optically transfer additional status information, e.g. firmware version, rotor offsets, etc. The azimuth θ_{PD_n} and elevation ϕ_{PD_n} angle for every photodiode PD_n can be calculated using the time difference Δt between the rising edge of one of the synchronization pulses t_1 or t_3 and the rising edge of the laser sweep t_5 as shown in Equation 1. The azimuth θ_{PD_n} is the angle in the XY-plane measured from the positive X-axis and elevation ϕ_{PD_n} is the angle in the XZ-plane measured from the positive X-axis. This deviates from the classic definition in a spherical coordinate system [36]–[42].

$$\begin{aligned} \Delta t &= \begin{cases} t_5 - t_1, & \text{if } 104\,\mu\text{s} \geq t_2 - t_1 \geq 62\,\mu\text{s} \\ t_5 - t_3, & \text{if } 104\,\mu\text{s} \geq t_4 - t_3 \geq 62\,\mu\text{s} \end{cases} \\ \theta_{PD_n} &= -\Delta t \cdot 60 \cdot 360 + 90^\circ \\ \phi_{PD_n} &= \Delta t \cdot 60 \cdot 360 - 90^\circ \end{aligned} \tag{1}$$

Whereas a prior implementation sampled the IR information at a regular interval and parsed the lighthouse data in post processing, our current firmware implementation is able to parse the information of the three photodiode receivers in real-time. This real-time execution was achieved by implementing a free-running 1-µs clock on the STM32F4 of which the counter value is added to a shift register with every rising or falling edge of the received IR pulses. With every new entry, the content of shift register will be shifted and checked for the appropriate time intervals that in turn triggers the calculation for either the azimuth or elevation. The 1-µs clock that was used in this process corresponds to measuring the lighthouse data with a resolution of 0.04°. The data will then be transferred through a UART-interface to the ESP8266 Wi-Fi SoC.

Despite the benefit of having wireless data acquisition capabilities, the problem of inter-node synchronization arises. The synchronization between the different nodes is crucial for the intended use-case of human body pose estimation. Unsynchronized data can result in body pose estimations where individual body parts appear to be lagging behind. This might even entirely disrupt the estimation technique. In order to

alleviate this issue every individual WBSN node will request a Network Time Protocol (NTP) timestamp from one of the available NTP servers. Within the specification of the NTP protocol it is stated that these timestamps are represented as a 64-bit fixed-point number, in seconds relative to 0000 UT on 1 January 1900 of which there is an integer part and a fractional part [43], [44]. This fractional part brings about a free-running 1-ms clock on the server side that can be polled. Once the NTP timestamp is received, the internal clock of the ESP8266 will maintain the time with microsecond precision only to refresh its NTP timestamp at larger intervals.

These microsecond timestamps are appended to every data point that is received from the STM32F4 before transmitting the data wirelessly through a TCP connection to a local server which collects all of the data. When we look into the collected data, it is clear that it is very unlikely to have data points between the different WBSN nodes with exactly the same timestamp. Due to our implementation where the nodes will sequentially initiate a connection to the TCP server, the first and/or last data point of the nodes will not be perfectly aligned either. By using linear interpolation on the collected data of every individual node between a common start and end timestamp, a synchronous data set is created with a fixed 100-ms interval.

III. SENSOR NODE MODEL, HUMAN BODY MODEL & PROBABILISTIC POSE ESTIMATION

Once the synchronous hardware architecture was developed and verified, its sensor data needed to be integrated into the processing algorithm in order to achieve the actual body pose estimates. To facilitate the sensor integration and further development of the pose estimation processing algorithm, we composed a model for the sensor node.

A. SENSOR NODE MODEL

Composing a model of the WBSN node, requires the characterization of the sensor in terms of the noise distribution, in this case on the azimuth and elevation data. By measuring the lighthouse data for every photodiode in various sensor orientations, the noise distribution is reflected in the actual standard deviation on the data. Using a FLIR Motion Control E46 Pan-Tilt Unit (PTU) [45], we were able to rotate a WBSN node mounted on the PTU with a given pan and tilt angle. In that specific orientation, 3600 data points were measured before moving to a new pan/tilt orientation. These measurements ranged from $-60°$ to $60°$ in pan angle and from $-30°$ to $30°$ tilt angle. When processing the lighthouse data for every orientation, the standard deviation (SD) of both azimuth and elevation were calculated for the individual photodiode. Figure 3 shows the noise distribution of the data of one of the three photodiodes. It is shown that the SD for all of the data varies between $0°$ and $0.1°$ in both the azimuth and elevation. If we calculate the mean standard deviation of these noise distributions, the mean SD for azimuth equals $0.0156°$ and $0.0128°$ for elevation. The data of the other photodiodes is comparable to these values and

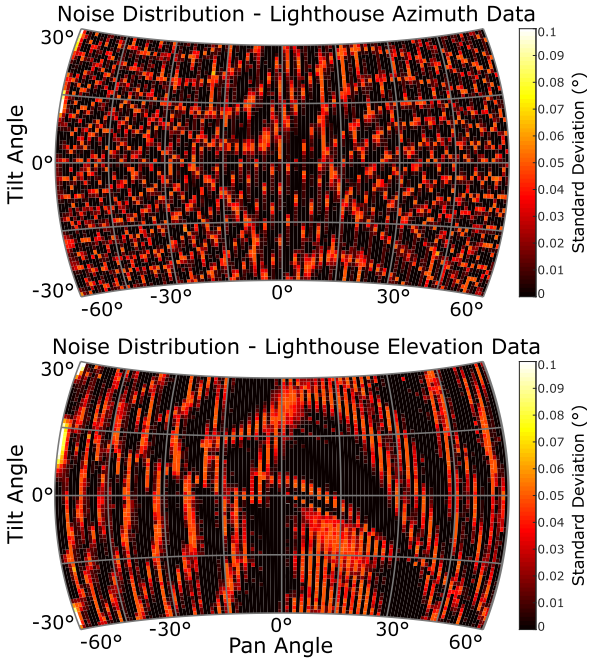

FIGURE 3. Using a FLIR E46 pan-tilt unit, which spurs accuracies up to $0.129°$, a WBSN node was oriented with various pan and tilt angles. Within a given range of pan and tilt angles the lighthouse azimuth and elevation data was measured which allowed us to establish the noise distributions for this sensor modality. Every data point represents the standard deviation on either the measured azimuth or elevation data for one of the photodiodes fitted on the WBSN node. The noise distributions for the other photodiodes were comparable and hence not shown in this figure.

therefore not mentioned or shown in Figure 3. Although the noise on the sensor data is almost negligible, it does allow us to simulate realistic sensor data. Though some geometrical patterns appear in the plots of Figure 3 we did not take them into account, as they are not consistent for all photodiodes and given the low values of the standard deviations. The simulations allows us to develop the required techniques and algorithms for establishing the actual estimation of the body poses without the need of performing numerous and time consuming experiments.

B. HUMAN BODY MODEL

In our previous work [24]–[27], a body pose was established by directly using the position and orientation (6DoF) of the individual measurement system(s). The pose of the human body or the pose of a subset of the body can be described as an interconnected chain of body parts with a given size and a point in 3D-space, that functions as the body's origin. Figure 4 panel a) shows an articulated lower body with $\vec{P}_B^w$ as the origin to which all other body parts are connected, defined in a right-handed world coordinate system that has its origin in $\vec{P}_O^w$. The superscript w indicates that this point is defined in the world coordinate system instead of a relative coordinate system, indicated with the superscript r. The body parts themselves can pivot around their respective joints that in turn affect the orientation of subsequent body parts. Since we are interested in estimating human body poses, a parametric human body model was created which incorporates (for

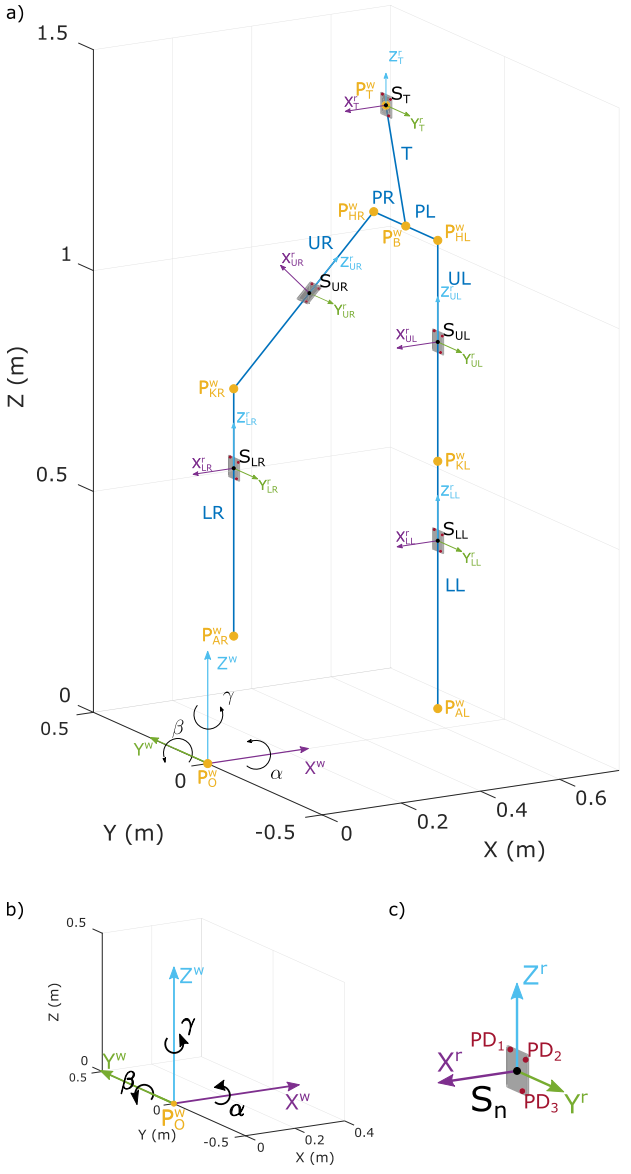

FIGURE 4. a) Human body model of an articulated lower body with $\vec{P}^w_B$ as the origin to which all other body parts are connected in a right-handed coordinate system with its origin in $\vec{P}^w_O$. The different body parts are an interconnected chain with a start and end point P relating to their human body counterparts. The sensors, designated with a capital S, are represented by a 3D-model of the PCB on which the photodiodes are indicated together with the center of the WBSN node. The center of the nodes correspond to the origin of their relative coordinate system, shown with its X, Y and Z axes. b) Zooms in on the origin of the world coordinate system and clearly shows the principal X, Y and Z axes and the rotations about these axes α, β and γ. c) Shows one of the WBSN nodes with its three photodiodes PD_1, PD_2 and PD_3 and center which corresponds to the origin of its relative coordinate system.

the time being) the lower limbs and torso. The parameters for the model consist of the physical size of each body part, their respective minimum and maximum rotations in either X, Y and Z in regard to the pivot point and the sensor placement on the body parts. Panel b of Figure 4 zooms in on the origin of the world coordinate system to clearly display how the X, Y and Z principal axes are oriented. This panel also shows the rotations α, β and γ in regard to these axes. The body consists of 7 parts: the torso (T), the left and right part of the pelvis (PL and PR), the upper left and right legs (UL and UR), the lower left and right legs (LL and LR).

These body parts each have a start and an end point which in most cases serve as joints, besides $\vec{P}^w_B$ these points are designated by an acronym derived from the name of the corresponding body part: the sternum ($\vec{P}_S$), the left and right hip ($\vec{P}^w_{HL}$ and $\vec{P}^w_{HR}$), the left and right knee ($\vec{P}^w_{KL}$ and $\vec{P}^w_{KR}$), the left and right ankle ($\vec{P}^w_{AL}$ and $\vec{P}^w_{AR}$). The sensors in Figure 4 are designated with a capital S with the body part they are attached to as their subscript, e.g. S_T is the sensor placed on the torso. Each sensor is represented using a 3D-model of the PCB on which the photodiodes are indicated together with the center of the PCB and its principal axes.

Our human body model, which consists of the aforementioned components, is an interconnected kinematic chain that is modeled as a set of matrix equations. As an example the equations that define the lower right joints $\vec{P}^w_{HR}$, $\vec{P}^w_{KR}$ and $\vec{P}^w_{AR}$ are given in Equation 2:

$$\begin{cases} \vec{P}^w_{HR} = \vec{P}^w_B + R^{\alpha,\beta,\gamma}_B \cdot \vec{V}_{PR} \\ \vec{P}^w_{KR} = \vec{P}^w_{HR} + R^{\alpha,\beta,\gamma}_B \cdot R^{\alpha,\beta,\gamma}_{UR} \cdot \vec{V}_{UR} \\ \vec{P}^w_{AR} = \vec{P}^w_{KR} + R^{\alpha,\beta,\gamma}_B \cdot R^{\alpha,\beta,\gamma}_{UR} \cdot R^{\alpha,\beta,\gamma}_{LR} \cdot \vec{V}_{LR} \end{cases}$$
$$\vec{V}_{PR} = \begin{bmatrix} 0 \\ -d_{PR} \\ 0 \end{bmatrix}, \vec{V}_{UR} = \begin{bmatrix} 0 \\ 0 \\ -d_{UR} \end{bmatrix}, \vec{V}_{LR} = \begin{bmatrix} 0 \\ 0 \\ -d_{LR} \end{bmatrix} \quad (2)$$

with R a 3D-rotation matrix given by the body parts' parent rotation defined by α, β and γ and a 3D-translation vector $\vec{V}$ defined by the size of the body part d. In the example of $\vec{P}^w_{KR}$ the point in world coordinates will be defined by the joint of the node $\vec{P}^w_{HR}$, the combined rotations of the pelvis and upper right leg (which corresponds to the product of the matrices $R^{\alpha,\beta,\gamma}_B$ and $R^{\alpha,\beta,\gamma}_{UR}$) and the translation vectors $\vec{V}_{UR}$. This vector equals to a negative displacement d_{UR} in the Z-axis that corresponds to the actual length of the upper right leg. This set of equations is the same for the left portion of the body and can be expanded for the other body parts.

To introduce the WBSN sensor nodes attached to the body parts into the model, the node's attributes are first defined in their relative coordinate system with the center of the PCB as its origin. In this case, the configuration of the photodiode array S^r_n is described by as a 3x3-matrix:

$$S^r_n = \begin{bmatrix} X^r_{PD_1} & X^r_{PD_2} & X^r_{PD_3} \\ Y^r_{PD_1} & Y^r_{PD_2} & Y^r_{PD_3} \\ Z^r_{PD_1} & Z^r_{PD_1} & Z^r_{PD_3} \end{bmatrix}$$

with X^r_{PD}, Y^r_{PD} and Z^r_{PD} the relative coordinates of PD_1, PD_2 and PD_3. In order to transform these relative coordinates to the world coordinate system, information regarding the placement of the sensor on the subject's body is required. This corresponds to defining a displacement vector $\vec{V}_{S_n}$ relative to the body part's parent joint. Equation 3 demonstrates how the

sensors' world coordinates are calculated:

$$\begin{cases} S^w_{UR} = P^w_{HR} + R^{\alpha,\beta,\gamma}_B \cdot R^{\alpha,\beta,\gamma}_{UR} \cdot (S^r_{UR} + V_{S_{UR}}) \\ S^w_{LR} = P^w_{KR} + R^{\alpha,\beta,\gamma}_B \cdot R^{\alpha,\beta,\gamma}_{UR} \cdot R^{\alpha,\beta,\gamma}_{LR} \cdot (S^r_{LR} + V_{S_{LR}}) \\ S^w_{UL} = P^w_{HL} + R^{\alpha,\beta,\gamma}_B \cdot R^{\alpha,\beta,\gamma}_{UL} \cdot (S^r_{UL} + V_{S_{UL}}) \\ S^w_{LL} = P^w_{KL} + R^{\alpha,\beta,\gamma}_B \cdot R^{\alpha,\beta,\gamma}_{UL} \cdot R^{\alpha,\beta,\gamma}_{LL} \cdot (S^r_{LL} + V_{S_{LL}}) \\ S^w_T = P^w_B + R^{\alpha,\beta,\gamma}_B \cdot R^{\alpha,\beta,\gamma}_T \cdot (S^r_T + V_{S_T}) \end{cases} \quad (3)$$

with $V_{S_n} = [\vec{V}_{S_n}|\vec{V}_{S_n}|\vec{V}_{S_n}]$ for every sensor array configuration S_n and $P^w_n = [\vec{P}^w_n|\vec{P}^w_n|\vec{P}^w_n]$ for every joint $\vec{P}^w_n$ to which the displacement vectors $\vec{V}_S$ are referred to. The displacement vectors $\vec{V}_S$ can also accommodate other translations that are not in the same direction as its subsequent body part, e.g. due to body tissue. $R^{\alpha,\beta,\gamma}$ represent the rotations of the subsequent body parts and S^r represents the sensor configuration. These equations yield the world coordinates S^w of all WBSN nodes and their sensor elements in a Cartesian 3D-world coordinate system. The individual sensor coordinates S^w of every WBSN node can thus be described as a 3x3-matrix that consists of the X, Y and Z coordinates. The combination of all S^w can be regarded as the sensor system state SS^w_S which can be written as a 3x15-matrix:

$$SS^w_S = \left[S^w_{UR} \mid S^w_{UL} \mid S^w_{UL} \mid S^w_{LL} \mid S^w_T\right]$$

Next, the position and orientation of the HTC Vive base stations, LH_A and LH_B, are defined in the world coordinate system. This information is necessary since the actual measured lighthouse sensor data is relative to either LH_A or LH_B. These points are defined by $\vec{P}^w_{LH}$, which describes the 3D-position (X, Y and Z), and a 3D-rotation (α, β and γ) that can be used to construct a rotation matrix $R^{\alpha,\beta,\gamma}_{LH}$. The sensor system state SS^r_S can thus be calculated by applying the rotation matrix $R^{\alpha,\beta,\gamma}_{LH}$ and a translation with $P^w_{LH} = [\vec{P}^w_{LH}|\vec{P}^w_{LH}|\vec{P}^w_{LH}]$ to the individual sensor coordinates of SS^w_S as shown in the following Equation:

$$SS^{r_{LH}}_S = P^w_{LH} + R^{\alpha,\beta,\gamma}_{LH} \cdot SS^w_S$$

The result is two 3x15 matrices $SS^{r_{LH_A}}_S$ and $SS^{r_{LH_B}}_S$ that contain the sensor coordinates in a relative Cartesian coordinate system with their origin defined by $\vec{P}^w_{LH_A}$ and $\vec{P}^w_{LH_B}$. As a last step (to translate the sensor coordinate data into lighthouse azimuth and elevation data) every column of either matrix $SS^{r_{LH}}_S$, containing Cartesian coordinates, can be converted to its spherical counterpart of which the range is discarded. As mentioned before, the HTC Vive base station's architecture deviates from the traditional spherical coordinate system definition. The HTC Vive lighthouse azimuth θ_{LH} and elevation ψ_{LH} data is more closely approximated using the following equations that make use of the four-quadrant inverse tangent function ($\tan^{-1}$):

$$\begin{cases} \theta_{LH}(k) = \tan^{-1} \dfrac{SS^{r_{LH}}_S(Y,k)}{SS^{r_{LH}}_S(X,k)} \\ \psi_{LH}(k) = \tan^{-1} \dfrac{SS^{r_{LH}}_S(Z,k)}{SS^{r_{LH}}_S(X,k)} \end{cases}$$

where the indices of the $SS^{r_{LH}}_S$ argument refer to the row and column of the matrix that correspond to either the X, Y or Z sensor coordinate and k the sensor's identifier. When applied to both $SS^{r_{LH_A}}_S$ and $SS^{r_{LH_B}}_S$, two 2x15-matrices $M^c_{LH_A}$ and $M^c_{LH_B}$ are calculated (hence the superscript c), which in turn can be written as a combined 2x30-matrix M^c_{LH}:

$$M^c_{LH_A} = \begin{bmatrix} \theta_{S_1} & \theta_{S_2} & \cdots & \theta_{S_{15}} \\ \psi_{S_1} & \psi_{S_2} & \cdots & \psi_{S_{15}} \end{bmatrix}$$
$$M^c_{LH_B} = \begin{bmatrix} \theta_{S_1} & \theta_{S_2} & \cdots & \theta_{S_{15}} \\ \psi_{S_1} & \psi_{S_2} & \cdots & \psi_{S_{15}} \end{bmatrix}$$
$$M^c_{LH} = \left[M^c_{LH_A}, M^c_{LH_B}\right]$$

C. PROBABILISTIC POSE ESTIMATION

Up to this point, we have established a forward parametric human body model that can be seen as a kinematic chain which can be used to generate sensor data M^c_{LH} based on the position of the HTC Vive base stations $\vec{P}^w_{LH}$, the sensor configuration S^r, displacement vectors $\vec{V}$ that define either size of the body parts or the placement of the sensors, a model's origin point $\vec{P}^w_B$ and rotations of the body parts $R^{\alpha,\beta,\gamma}$. While a number of these parameters are dependent on the measurement setup and test subject, the origin point $\vec{P}^w_B$ and rotations of the body parts α, β, γ are the variables which are used to estimate the actual pose of the subject throughout a simulation or experiment.

Since we have a priori information concerning which rotations can be expected for every joint, a number of parameters can be discarded resulting in a 14-element vector $\vec{\Omega}$:

$$\vec{\Omega} = \left[\vec{P}^w_B(X), \vec{P}^w_B(Y), \vec{P}^w_B(Z), \alpha_B, \beta_B, \gamma_B, \beta_{UR}, \gamma_{UR}, \beta_{LR}, \beta_{UL}, \gamma_{UL}, \beta_{LL}, \beta_T, \gamma_T\right]$$

This vector can be used to generate a sensor system pose, and consequently the sensor azimuth and elevation data $M^c_{LH}(\vec{\Omega})$ that is the input for our probabilistic pose estimation algorithm. This algorithm will minimize the difference between the measured lighthouse azimuth and elevation data M^m_{LH} and the calculated azimuth and elevation data $M^c_{LH}(\vec{\Omega})$. To perform the minimization, a likelihood function $\mathcal{L}(\vec{M}^m_{LH}|\vec{\Omega})$ for a measurement M^m_{LH} given a parameter vector $\vec{\Omega}$ is defined. This likelihood function assumes Gaussian error distributions on the measured data and can be written as follows using the vectorized versions $\vec{M}^m_{LH}$ and $\vec{M}^c_{LH}(\vec{\Omega})$ of the matrices M^m_{LH} and $M^c_{LH}(\vec{\Omega})$:

$$\mathcal{L}(\vec{M}^m_{LH}|\vec{\Omega}) = e^{\left[-\frac{1}{2}\cdot(\vec{M}^m_{LH}-\vec{M}^c_{LH}(\vec{\Omega}))^T \cdot \mathbf{\Sigma_m^{-1}} \cdot (\vec{M}^m_{LH}-\vec{M}^c_{LH}(\vec{\Omega}))\right]}$$

with $\mathbf{\Sigma_m}$ being the distribution's covariance matrix that is set to be a scaled identity matrix multiplied with a noise distribution σ_m for the azimuth and elevation:

$$\mathbf{\Sigma_m} = \sigma_m \cdot I$$

Using the likelihood function a posterior probability function for the parameter vector $\vec{\Omega}$ can be calculated given a

measurement $\vec{M}^m_{LH}$, utilizing Bayes rule:

$$P(\vec{\Omega}|\vec{M}^m_{LH}) = \frac{\mathcal{L}(\vec{M}^m_{LH}|\vec{\Omega}) \cdot P(\vec{\Omega})}{\sum_{\vec{\Omega}} \left[\mathcal{L}(\vec{M}^m_{LH}|\vec{\Omega}) \cdot P(\vec{\Omega})\right]}$$

with $P(\vec{\Omega})$ the prior distribution function for $\vec{\Omega}$ which correlates to a set of constraints for the parameter vector. This allows further utilizing the a priori information regarding the rotation ranges of the joints. To achieve the human body pose estimates, the parameter vector $\vec{\Omega}_{est}$ will be estimated by minimizing the negative logarithm of the posterior probability function using an unconstrained non-linear minimization function:

$$\vec{\Omega}_{est} = \arg\min \left\{ -\log \left[P(\vec{\Omega}|\vec{M}^m_{LH} \right] \right\}$$

IV. SIMULATED RESULTS

By combining these sets of equations in conjunction with our parametric human body model and probabilistic pose estimation algorithm, we are able to simulate the efficacy of the proposed human body pose estimation system. For multiple simulations an environment was set up in which two virtual HTC Vive base stations were positioned. A simulated lower human body, to which five WBSN nodes were attached, was described by defining the parameters of the human body model together with the sensor placement. By defining a motion/gait pattern the simulated test subject can move in the environment in a given time period sampled at a fixed interval. Every time step corresponds to a snapshot of the simulated subject's pose that was used as our ground-truth. Using our proposed models we can simulate WBSN lighthouse data to which sensor noise can be applied. The simulated measurement data will in turn be used as in the input for our pose estimation algorithm in combination with the parameters of the forward parametric human body model. In these simulations a walking trajectory was often chosen from the back of the simulated environment to the front where the HTC Vive base stations were positioned. Figure 5 shows a representation of one of these simulation experiments. In this representation four snapshots were chosen in which the estimated pose is shown along the movement trajectory together with the ground-truth pose as an overlay. The lighthouses in the environment are indicated with an $\times$ at the corresponding position.

As can be seen in Figure 5, the ground-truth poses and estimated poses differ only slightly even when we add more sensor noise to the simulated measurements than we have established through our sensor characterization. On the one hand, the noise rejection of our proposed method can be attributed to the use of the parametric human body model (PHBM) which constrains the solution space due to the kinematic chain. On the other hand, the proposed model also limits the rotation ranges of the joints. Some rotation ranges can even be discarded thus reducing the parameter vector $\vec{\Omega}$ to 14 parameters for an articulated lower human body equipped with 5 WBSN nodes. In previous work where the 6DoF pose for every individual node (IN) was estimated to establish a

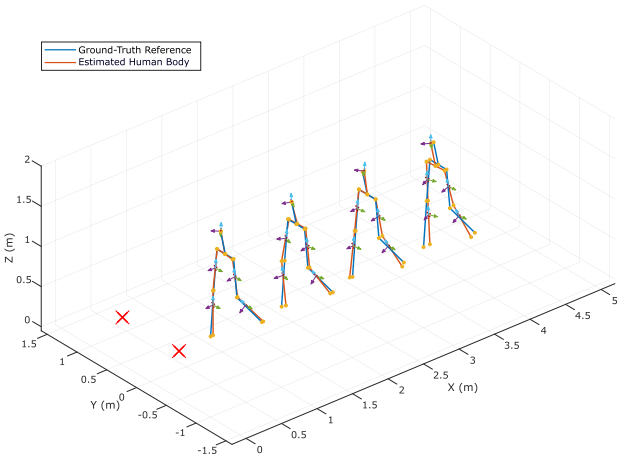

FIGURE 5. Visual representation of one of the simulations that were used to verify the proposed algorithms and models. In this simulation a lower human body was outfitted with 5 WBSN nodes, the former and the latter were described in the human body model by defining its parameters and sensor placement. The simulated test subject walked from the back to the front of the defined environment, in which two lighthouses were positioned. Both the estimated pose as the ground-truth pose are drawn in this representation.

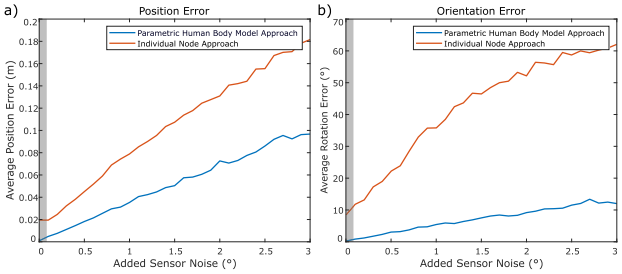

FIGURE 6. The efficacy of our proposed pose estimation technique based on a parametric human body model that incorporates a kinematic chain to estimating a body pose by using a combination of the 6DoF poses of individual nodes was quantified in a simulation that added cumulative sensor noise. As performance metrics the average error on both the position and the orientation were used. Panel a) represents the average error on the position whereas panel b) shows the average orientation error. It is shown that in both cases the parametric human body model approach boasts lower average errors in general and is less susceptible to sensor noise. The region of interest is indicated with a gray background in both panels.

body pose, the joint parameter vector for estimating the same articulated lower human body with an equal amount of sensor nodes would consist of 30 parameters (6DoF * 5 nodes).

In order to quantify the efficacy of using either parameter vector $\vec{\Omega}_{PHBM}$ (consisting of 14 parameters) or $\vec{\Omega}_{IN}$ (consisting of 30 parameters), the average position and orientation errors were compared with added cumulative sensor noise. Whereas the individual node approach does not benefit from the rotational constraints nor a kinematic chain, the same probabilistic pose estimation algorithm was used to approximate the human body pose. Using the aforementioned simulation environment, these two approaches could be tested of which the results are shown in Figure 6 where panel a) shows the average position error and b) the average orientation error. These results clearly show that a human body model with a kinematic chain approach, which reduces the parameter vector $\vec{\Omega}$, has an overall much lower average error on both

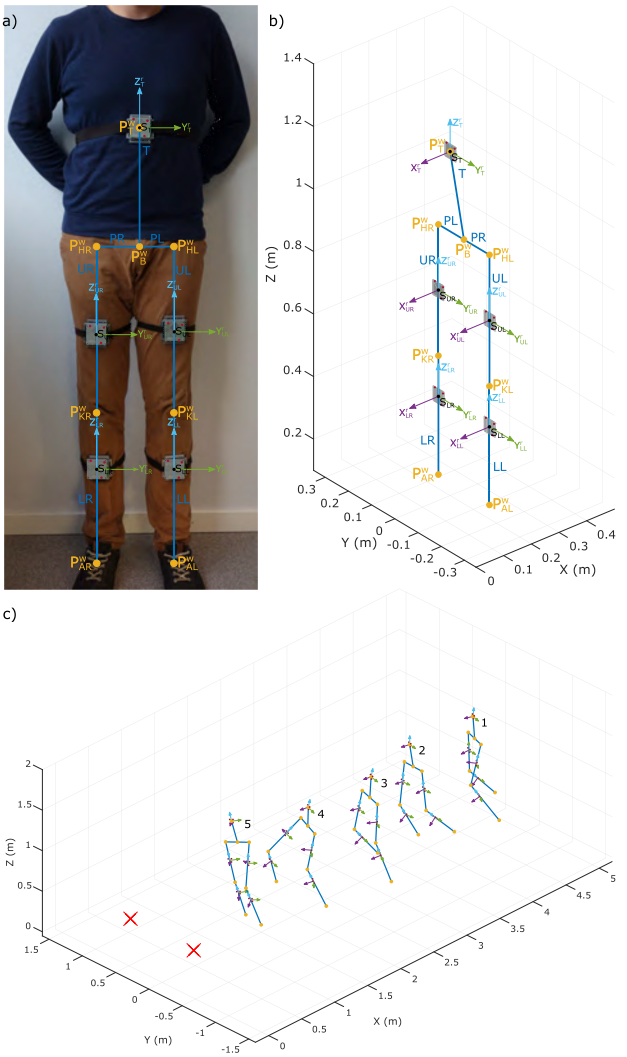

FIGURE 7. **In a) our test subject was equipped with five WBSN nodes to the upper legs, lower legs and torso. Based on the node placement on the body and on the physical properties of the test subject, an estimated body pose was generated that is shown as an overlay. Panel b) shows the same estimated pose of the test subject by itself from a different viewpoint. Panel c) Shows five snapshots of body pose estimates based on a recorded motion pattern. The first three snapshots illustrate the poses during a normal gait pattern in a straight line while the fourth and fifth snapshot display the test subject lifting its right and left leg. While a ground-truth reference could not be recorded at this time, the poses can be easily distinguished.**

the position and orientation. Additionally the individual node approach is more susceptible to sensor noise, especially the average orientation error quickly escalates. These results prove that our proposed parametric human body model is highly resistant to sensor noise. This feature is desirable in a system that requires high accuracy and precision in its pose estimates.

V. EXPERIMENTAL RESULTS

Trough iterative development and extensive simulations we were able to create the algorithms that perform the human body pose estimations using the generated gait patterns and simulated sensor data with added sensor noise distributions. These simulations also enabled us to quantify the efficacy of the proposed technique. A number of experiments were performed to verify the feasibility of the developed human body model, probabilistic pose estimation approach and simulations in real-world circumstances. An office environment, which measures 6.2 m by 3.4 m by 3.1 m, was used as our test environment. It was equipped with two HTC Vive base stations and an off-the-shelve Wi-Fi router. Five WBSN nodes were attached to a human test subject's lower body, i.e. the upper left and right legs, lower left and right legs and torso as shown in Figure 7 panel a) with an overlay of the estimated body pose by using the parametric human body model. Panel b) of Figure 7 displays the same estimated body pose by itself from a different viewpoint.

The test subject walked from the back of the test environment towards the front of the room where the lighthouses were set up, marked with an $\times$ in Figure 7 panel c). Throughout this recorded motion a number of motions and stances were used, at first the test subject walked in a straight line using a normal gait pattern after which the test subject raised its right leg, switched to lifting its left leg and finishing in a standing pose. Figure 7 panel c) displays five chosen snapshots of the estimated poses based on the recorded data. In the first three snapshots the gait pattern is shown while snapshot four and five display lifting respectively the right and left leg. These estimated body poses can be easily distinguished and certainly appear to reflect the reality.

A ground-truth reference that confirms the realism of our estimated body poses however was not accomplished throughout our real-world experiment due to practical concerns. While a Qualisys motion capture system was available to establish a ground-truth, the cameras used by such a measurement system emit infrared emissions that interfere with the infrared emissions emitted by the HTC Vive base stations. This IR interference disrupts the processing of the photodiode information thus rendering the WBSN nodes virtually void of the sensor information. We are currently working on a solution to alleviate the lack of a ground-truth reference.

VI. DISCUSSION, CONCLUSIONS AND FUTURE WORK

By introducing a new hardware architecture based on a WBSN topology we have created a novel approach to human body pose estimation in a low-cost yet accurate and precise fashion. The basis for our approach is powerful yet power-efficient hardware that combines three sensor modalities. These sensors (optical, acoustic and inertial) can be used to complement one another to overcome their inherent flaws, e.g. non-line-of-sight, integration drift, etc. by applying sensor fusion techniques. In this paper, we limited ourselves to only using a single modality, i.e. the optical detection of emitted IR pulses and laser plane sweeps. Through its scalable architecture and wireless data transfer capabilities combined with NTP microsecond timestamps, which allows inter-node synchronization, a significant step was been taken towards attaining full body pose measurements and estimations. As a future addition to fully utilize and optimize the captured lighthouse data, the synchronization pulses can be parsed to gain

additional information of the HTC Vive base stations. This information contains e.g. device specific calibration offsets of the horizontal and vertical rotors.

While the redesigned hardware proves to be a valuable contribution, this first iteration of the parametric human body model also shows great promises for the body pose estimates. Given the structure of the kinematic chain, other joints and body parts can be easily added with their respective rotational ranges and physical sizes. Although currently only the sensor model for the HTC Vive sensor is implemented, the other sensor modalities will follow to further improve the robustness, accuracy and precision of the pose estimates. The sensor processing and pose estimation techniques could be further optimized in future work as well. In this work single snapshots of sensor data are processed to attain the body poses while time-sequence processing could be used instead. This type of processing could be achieved by applying a moving-window technique on the sensor data or by using a particle filter in conjunction with our probabilistic pose estimator.

Although we have established a simulation environment that allows us to produce realistic sensor data in combination with the measured noise distributions, experiments where a ground-truth reference can also be recorded are needed for benchmarking purposes and further validation of the developed algorithms. This will give us a better insight into the real accuracy and precision of our proposed human body pose estimation system. We believe this can be achieved using our Qualisys motion capture system in combination with active IR LED markers, instead of passive markers, placed at known positions on the various WBSN sensor nodes. By using these active markers, the IR emissions of the Qualisys cameras can be disabled thus allowing us to capture the HTC Vive IR sweeps and pulses to obtain the WBSN lighthouse sensor data and simultaneously track the position and orientation of the sensor nodes with the Qualisys system.

REFERENCES

[1] R. A. Khan and A.-S. K. Pathan, "The state-of-the-art wireless body area sensor networks: A survey," *Int. J. Distrib. Sensor Netw.*, vol. 14, no. 4, Apr. 2018, Art. no. 1550147718768994. [Online]. Available: http://journals.sagepub.com/doi/10.1177/1550147718768994

[2] S. Sharma, M. M. Tripathi, and V. M. Mishra, "Survey paper on sensors for body area network in health care," in *Proc. Int. Conf. Emerg. Trends Comput. Commun. Technol. (ICETCCT)*, Nov. 2017, pp. 1–6. [Online]. Available: http://ieeexplore.ieee.org/document/8280299/

[3] J. Kropff *et al.*, "Accuracy of two continuous glucose monitoring systems: A head-to-head comparison under clinical research centre and daily life conditions," *Diabetes, Obesity Metabolism*, vol. 17, no. 4, pp. 343–349, Apr. 2015. [Online]. Available: http://doi.wiley.com/10.1111/dom.12378

[4] H. A. A. Sabti and D. V. Thiel, "Self-calibrating body sensor network based on periodic human movements," *IEEE Sensors J.*, vol. 15, no. 3, pp. 1552–1558, Mar. 2015. [Online]. Available: http://ieeexplore.ieee.org/document/6936300/

[5] L. Jiao, H. Wu, R. Bie, A. Umek, and A. Kos, "Multi-sensor golf swing classification using deep CNN," *Procedia Comput. Sci.*, vol. 129, pp. 59–65, 2018. [Online]. Available: http://linkinghub.elsevier.com/retrieve/pii/S1877050918302692

[6] E. van Breda, S. Verwulgen, W. Saeys, K. Wuyts, T. Peeters, and S. Truijen, "Vibrotactile feedback as a tool to improve motor learning and sports performance: A systematic review," *BMJ Open Sport Exerc. Med.*, vol. 3, no. 1, Jul. 2017, Art. no. e000216. [Online]. Available: http://bmjopensem.bmj.com/lookup/doi/10.1136/bmjsem-2016-000216

[7] S. Verwulgen *et al.*, "Accuracy and efficiency validation of a helmet mounted vibrotactile feedback system for aerodynamic head position during cycling," in *Proc. Int. Conf. Appl. Hum. Factors Ergonom.* Cham, Switzerland: Springer, Jul. 2018, pp. 85–93. [Online]. Available: http://link.springer.com/10.1007/978-3-319-60639-2_9

[8] P. Van de Walle *et al.*, "Age-related changes in arm motion during typical gait," *Gait Posture*, vol. 66, pp. 51–57, Oct. 2018.

[9] G. M. Rozanski, J. S. Wong, E. L. Inness, K. K. Patterson, and A. Mansfield, "Longitudinal change in spatiotemporal gait symmetry after discharge from inpatient stroke rehabilitation," *Disab. Rehabil.*, pp. 1–7, 2019. doi: 10.1080/09638288.2018.1508508.

[10] T. Van Criekinge *et al.*, "Age-related differences in muscle activity patterns during walking in healthy individuals," *J. Electromyography Kinesiology*, vol. 41, pp. 124–131, Aug. 2018.

[11] A. R. Anwary, H. Yu, and M. Vassallo, "An automatic gait feature extraction method for identifying gait asymmetry using wearable sensors," *Sensors*, vol. 18, no. 2, p. 676, Feb. 2018. [Online]. Available: http://www.mdpi.com/1424-8220/18/2/676

[12] A. A. Jafarnezhadgero, M. Majlesi, H. Etemadi, and D. G. E. Robertson, "Rehabilitation improves walking kinematics in children with a knee varus: Randomized controlled trial," *Ann. Phys. Rehabil. Med.*, vol. 61, no. 3, pp. 125–134, May 2018. [Online]. Available: http://www.ncbi.nlm.nih.gov/pubmed/29476933

[13] A. W. Titus, S. Hillier, Q. A. Louw, and G. Inglis-Jassiem, "An analysis of trunk kinematics and gait parameters in people with stroke," *Afr. J. Disab.*, vol. 7, pp. 1–6, Mar. 2018. [Online]. Available: http://www.ajod.org/index.php/AJOD/article/view/310

[14] A. Toshev and C. Szegedy, "DeepPose: Human pose estimation via deep neural networks," in *Proc. IEEE Comput. Soc. Conf. Comput. Vis. Pattern Recognit.*, Jun. 2014, pp. 1653–1660.

[15] R. A. Güler, N. Neverova, and I. Kokkinos. (2018). "DensePose: Dense human pose estimation in the wild." [Online]. Available: https://arxiv.org/abs/1802.00434

[16] I. H. López-Nava and A. Muñoz-Meléndez, "Wearable inertial sensors for human motion analysis: A review," *IEEE Sensors J.*, vol. 16, no. 22, pp. 7821–7834, Nov. 2016. [Online]. Available: http://ieeexplore.ieee.org/document/7567551/

[17] M. Schepers, M. Giuberti, and G. Bellusci, "Xsens MVN: Consistent tracking of human motion using inertial sensing," Enschede, The Netherlands, Xsens, White Paper, Mar. 2018, pp. 1–8.

[18] A. Filippeschi, N. Schmitz, M. Miezal, G. Bleser, E. Ruffaldi, and D. Stricker, "Survey of motion tracking methods based on inertial sensors: A focus on upper limb human motion," *Sensors*, vol. 17, no. 6, p. 1257, Jun. 2017. [Online]. Available: http://www.mdpi.com/1424-8220/17/6/1257

[19] P. Kutilek, Z. Svoboda, O. Cakrt, K. Hana, and M. Chovanec, "Postural stability evaluation of patients undergoing vestibular Schwannoma microsurgery employing the inertial measurement unit," *J. Healthcare Eng.*, vol. 2018, Apr. 2018, Art. no. 2818063.

[20] D. Roetenberg, H. Luinge, and P. Slycke, "Xsens MVN: Full 6DOF human motion tracking using miniature inertial sensors," *Xsens Motion Technol. BV Tech. Rep.*, vol. 3, p. 9, Jan. 2009.

[21] T. Seel, J. Raisch, and T. Schauer, "IMU-based joint angle measurement for gait analysis," *Sensors*, vol. 14, no. 4, pp. 6891–6909, Jan. 2014. [Online]. Available: http://www.mdpi.com/1424-8220/14/4/6891/

[22] W. Flenniken, J. Wall, and D. Bevly, "Characterization of various IMU error sources and the effect on navigation performance," in *Proc. 18th Int. Tech. Meeting Satell. Division Inst. Navigat. (ION GNSS)*, 2005, pp. 1–12.

[23] M. Kok, J. D. Hol, and T. B. Schön, "Using inertial sensors for position and orientation estimation," *Found. Trends Signal Process.*, vol. 11, nos. 1–2, pp. 1–153, 2017. [Online]. Available: http://www.nowpublishers.com/article/Details/SIG-094

[24] D. Laurijssen, S. Truijen, W. Saeys, and J. Steckel, "Three sources, three receivers, six degrees of freedom: An ultrasonic sensor for pose estimation & motion capture," in *Proc. IEEE SENSORS*, Nov. 2015, pp. 1–4.

[25] D. Laurijssen, S. Truijen, W. Saeys, W. Daems, and J. Steckel, "An ultrasonic six degrees-of-freedom pose estimation sensor," *IEEE Sensors J.*, vol. 17, no. 1, pp. 151–159, Jan. 2017. [Online]. Available: http://ieeexplore.ieee.org/document/7592877/

[26] D. Laurijssen, S. Truijen, W. Saeys, W. Daems, and J. Steckel, "A flexible embedded hardware platform supporting low-cost human pose estimation," in *Proc. Int. Conf. Indoor Positioning Indoor Navigat. (IPIN)*, Oct. 2016, pp. 1–8. [Online]. Available: http://ieeexplore.ieee.org/document/7743682/

[27] D. Laurijssen, S. Truijen, W. Saeys, W. Daems, and J. Steckel, "Six-DoF pose estimation using dual-axis rotating laser sweeps using a probabilistic framework," in *Proc. Int. Conf. Indoor Positioning Indoor Navigat. (IPIN)*, Sep. 2017, pp. 1–8. [Online]. Available: http://ieeexplore.ieee.org/document/8115913/

[28] STMicroelectronics. (2018). *Overview STM32F427xx STM32F429xx Advanced ARM-Based 32-Bit MCUs*. [Online]. Available: http://www.st.com/resource/en/datasheet/stm32f429zi.pdf

[29] R. Kerstens, D. Laurijssen, and J. Steckel, "Low-cost one-bit MEMS microphone arrays for in-air acoustic imaging using FPGA's," in *Proc. IEEE SENSORS*, Oct./Nov. 2017, pp. 1–3. [Online]. Available: http://ieeexplore.ieee.org/document/8234087/

[30] Knowles Electronics. (2015). *SPH0641LU4H-1*. [Online]. Available: https://www.knowles.com/docs/default-source/model-downloads/sph0641lu4h-1-revb.pdf

[31] B. Sensortec. (2014). *Intelligent 9-Axis Absolute Orientation Sensor BNO055*. [Online]. Available: https://ae-bst.resource.bosch.com/media/_tech/media/datasheets/BST-BNO055-DS000.pdf

[32] M. F. Ruzaij, S. Neubert, N. Stoll, and K. Thurow, "Design and implementation of low-cost intelligent wheelchair controller for quadriplegias and paralysis patient," in *Proc. IEEE 15th Int. Symp. Appl. Mach. Intell. Inform. (SAMI)*, Jan. 2017, pp. 399–404.

[33] M. F. Ruzaij, S. Neubert, N. Stoll, and K. Thurow, "A speed compensation algorithm for a head tilts controller used for wheelchairs and rehabilitation applications," in *Proc. IEEE 15th Int. Symp. Appl. Mach. Intell. Inform. (SAMI)*, Jan. 2017, pp. 497–502.

[34] M. Romanov, P. Berghold, M. Frank, D. Rudrich, M. Zaunschirm, and F. Zotter, "Implementation and evaluation of a low-cost headtracker for binaural synthesis," in *Audio Engineering Society Convention 142*. 2017. [Online]. Available: http://www.aes.org/e-lib/browse.cfm?elib=18567

[35] Espressif Systems. (2018). *Esp8266Ex*. [Online]. Available: https://www.espressif.com/sites/default/files/documentation/0a-esp8266ex_datasheet_en.pdf

[36] D. R. Quiñones, G. Lopes, D. Kim, C. Honnet, D. Moratal, and A. Kampff, "HIVE tracker: A tiny, low-cost, and scalable device for sub-millimetric 3D positioning," in *Proc. 9th Augmented Hum. Int. Conf. (AH)*, Seoul, South Korea, 2018, pp. 9:1–9:8. doi: 10.1145/3174910.3174935.

[37] M. Kals, "Indoor navigation using the HTC vive base-stations," Sintef, Trondheim, Norway, Tech. Rep., 2017, pp. 1–35.

[38] D. C. Niehorster, L. Li, and M. Lappe, "The accuracy and precision of position and orientation tracking in the HTC vive virtual reality system for scientific research," *i-Perception*, vol. 8, no. 3, pp. 1–23, 2017.

[39] J. Egger *et al.*, "HTC Vive MeVisLab integration via OpenVR for medical applications," *PLoS ONE*, vol. 12, no. 3, pp. 1–14, 2017.

[40] M. Borges, A. Symington, B. Coltin, T. Smith, and R. Ventura, "HTC Vive: Analysis and accuracy improvement," in *Proc. IEEE/RSJ Int. Conf. Intell. Robots Syst. (IROS)*, 2018, pp. 2610–2615.

[41] S. Trendel, "A framework for motion analysis of anthropomimetic robots," Dept. Inform., Technische Universität München, Munich, Germany, 2018.

[42] S. Islam, B. Ionescu, C. Gadea, and D. Ionescu, "Indoor positional tracking using dual-axis rotating laser sweeps," in *Proc. IEEE Instrum. Meas. Technol. Conf.*, May 2016, pp. 1–6.

[43] D. L. Mills, *Network Time Protocol (NTP)*, document RFC 958, M/A-Com Linkabit, Network Working Group, Sep. 1985.

[44] D. L. Mills, "Internet time synchronization: The network time protocol," *IEEE Trans. Commun.*, vol. 39, no. 10, pp. 1482–1493, Oct. 1991.

[45] FLIR Commercial Systems. (2014). *Pan & Tilt Unit E46*. [Online]. Available: https://www.flir.eu/globalassets/imported-assets/document/ptu-e46-user-manual.pdf

DENNIS LAURIJSSEN (GS'18) received the M.Sc. degree in electrical engineering from Artesis Hogeschool, Belgium, in 2012. He is currently pursuing the Ph.D. degree with the CoSys Lab. After getting his M.Sc. degree, he joined the CoSys Lab, in 2012, for a brief period as a Researcher. In 2013, he pursued an opportunity at a startup company in San Francisco for a short internship, after which he started to work for the Centre for Care Technology, University of Antwerp, until 2015. His research interests include in-air ultrasonic systems, pose estimation systems, wireless communication, embedded (DSP) systems, and array signal processing.

WIM SAEYS was born in Brasschaat, Belgium, in 1982. He received the M.Sc. degree in physiotherapy and rehabilitation sciences from the University College of Antwerp, Belgium, in 2005, the M.Sc. degree in neurological rehabilitation from the University of Brussels, Belgium, in 2006, and the Ph.D. degree from the University of Antwerp, Belgium, in 2012. In the following years, he conducted research on the topic of gait analysis in combination with balance and posture control in people suffering from brain damage. He is currently with the rehabilitation hospital Revarte. He is also a Tenure Track Professor with the REVAKI Research Group, University of Antwerp.

STEVEN TRUIJEN received the M.Sc. and Ph.D. degrees. As the Chairman of the Department Rehabilitation Sciences and Physiotherapy (REVAKI), he works actively at the development and integration of the department REVAKI, Faculty of Medicine and Health Sciences, University of Antwerp. The focus of his research is to add value in health care by multidisciplinary cooperation, as a Core Member of StatUA, the core facility for Statistics of the University of Antwerp, a member of the Centre for Care Technology, University of Antwerp (CZT), and a Co-Promoter of the Multidisciplinary Motor Centre Antwerp (M^2OCEAN).

WALTER DAEMS (S'97–M'02–SM'18) was born in Wilrijk, Belgium, in 1971. He received the B.Sc. degree in electronics from the Katholieke Industriële Hogeschool Antwerpen, Hoboken, Belgium, in 1994, and the M.Sc. degree in electrical engineering and the Ph.D. degree from the Katholieke Universiteit Leuven, Leuven, Belgium, in 1996 and 2002, respectively. After a Postdoctoral Fellowship of the Fund for Scientific Research, Flanders, Belgium, he cofounded Kimotion Technologies, Inc. In 2006, he joined the Karel de Grote University College, Hoboken, where he was appointed as the Vice Dean of academic affairs. In 2013, he was one of the main founders of the Faculty of Applied Engineering at the University of Antwerp, Belgium. Since then, he has been an Associate Professor with the Faculty of Applied Engineering and the Chairman of the Faculty's Educational Board. As of 2018, he acts as the Vice Dean for education of the Faculty. He is a member of Staff of the Constrained Systems Lab. He is also active in the Centre for Care Technology, University of Antwerp. His research interests include digital signal and image processing and the implementation of these systems in embedded technology for application in industry and (health) care.

JAN STECKEL received the Dr.Ing. degree in electronic engineering from the Karel de Grote University College, Hoboken, in 2007, and the Ph.D. degree from the Active Perception Lab, University of Antwerp, in 2012. His Ph.D. dissertation was Array Processing for In-Air Sonar Systems - Drawing Inspirations From Biology. During this period, he developed state-of-the art sonar sensors, both biomimetic and sensor-array based. During his postdoctoral period, he was an Active Member of the Centre for Care Technology, University of Antwerp, where he was in charge of various healthcare-related projects concerning novel sensor technologies. In 2015, he became a tenure track Professor at the Constrained Systems Lab, University of Antwerp, where he researches sensors, sensor arrays, and signal processing algorithms using an embedded, constrained systems approach. He pursued industrial exploitation of the patented 3-D array sonar sensor that was developed in collaboration during his Ph.D. degree.